ORIGINAL RESEARCH ARTICLE

Influence of a Partial Substitution of Co by Fe on the Phase Stability and Fatigue Behavior of a CoCrWC Hard Alloy at Room Temperature

LUKAS BRACKMANN, JANNIK SCHUPPENER, ARNE RÖTTGER, and SEBASTIAN WEBER

The deformation-induced phase transition from fcc to hcp causes local embrittlement of the metal matrix in Cobalt-base alloys, facilitating subcritical crack growth under cyclic loading and reducing fatigue resistance. Our approach to increasing the fatigue life of Co-based hard alloys is to suppress the phase transition from fcc to hcp by an alloy modification that increases the stacking fault energy (SFE) of the metal matrix. Therefore, we substitute various contents (15, 25, and 35 mass pct) of Co by Fe and analyze the effect on the fatigue life and resistance against subcritical crack growth. Subcritical crack growth in the specimens takes place in a cyclic load test. The proceeding crack growth and the occurrence of phase transformations are monitored by scanning electron microscope (SEM) investigations and electron backscatter diffraction (EBSD). We determined an SFE of 35 mJ/m^2 at an iron content of 35 mass pct, which leads to a change of the main deformation mechanism from deformation-induced martensitic transformation to deformation twinning. Analysis of cyclically loaded specimens revealed that the resistance against subcritical crack growth in the metal matrix is facilitated with increasing Fe content, leading to a significant increase in fatigue life.

https://doi.org/10.1007/s11661-022-06700-7

I. INTRODUCTION

COBALT-BASE hard alloys, such as the various Stellites®, are commonly used for wear protection of components that are exposed to elevated temperatures during use.[1] In this work, however, we are focusing on optimizing Co-base hard alloys for wear-resistant applications at non-elevated temperatures, which at the same time demand a high fatigue resistance. This work is motivated by the superior fracture toughness of Co-base hard alloys (35 to 45 MPa $m^{1/2}$), compared to Fe-base (20 to 30 MPa $m^{1/2}$) or Ni-base (20 to 35 MPa $m^{1/2}$) alloys, along with high resistance against subcritical crack propagation.[2–4]

Applications that are specifically targeted by this research are built-up welded wear-protective coatings on abrasive-wear-loaded parts like tunneling tools or caterpillar shovels.[5] These applications comprise a load-collective consisting of abrasive wear, cyclic mechanical loading, and occasional mechanical overloading. Therefore, the used material has to contain a significant amount of hard phases in the form of carbides or borides to inhibit abrasive wear. At the same time, a sufficient fracture toughness is needed to avoid catastrophic fracture in the case of mechanical overloads. And lastly, to avoid material fatigue due to cyclic loading, a high resistance against subcritical crack propagations is required. The influence of elevated temperatures is less important, as for example in mechanized tunneling the temperature of the tunneling tools rarely exceeds 100 °C.

In previous work, we investigated the fatigue life of various hard alloys on Fe-, Ni-, and Co basis. Our results showed that the Co-base hard alloy Stellite® 6 achieved longer fatigue lifetimes (factor 3 to 4) than Ni-base hard alloys, which are nowadays commercially used for the previously mentioned applications. The high fatigue life of Stellite® 6 could be traced back to the advantageous combination of strength and toughness of the fcc metal matrix. However, due to localized deformation-induced phase transformation (DIMT)

LUKAS BRACKMANN, JANNIK SCHUPPENER, and SEBASTIAN WEBER are with the Chair of Materials Technology, Institute for Materials, Ruhr-Universität Bochum, Universitätsstraße 150, 44801, Bochum, Germany. Contact e-mail: brackmann@wtech.rub.de ARNE RÖTTGER is with the Chair for New Production Technologies and Materials, Bergische Universität Wuppertal, Bahnhofstraße 15, 42651, Solingen, Germany.
Manuscript submitted December 23, 2021; accepted April 20, 2022.
Article published online May 9, 2022

from fcc to hcp, embrittlement of the metal matrix occurred, which eventually facilitated crack propagation. This deformation-induced phase transformation was investigated by electron backscatter diffraction (EBSD) scans, which illustrated straight-lined crack propagation in locally transformed hcp channels in the metal matrix.[6]

In this work, we are investigating an approach to inhibit the stress-induced phase transformation in Stellite® 6 by increasing the stacking fault energy (SFE) of the Co-base metal matrix to increase the fatigue life.

Stacking faults are two-dimensional defects in the crystal lattice, which are created by splitting a dislocation into two Shockley partial dislocations, which enclose the stacking fault. The ability of a material to form stacking faults is controlled by its stacking fault energy. Alloys with low SFE have a larger tendency to form stacking faults compared to alloys with high SFE.[7] The Co-base metal matrix of Stellite® 6 has a low SFE of $< 15\ mJ/m^2$ and is, therefore, rich in stacking faults. These stacking faults are especially important, as they represent the nucleation points for the phase transformation from the fcc to the hcp lattice. Due to the relationship of the crystallographic directions between the fcc and the hcp lattice, the atomic layers with the wrong stacking sequence can be considered as an hcp nucleus.[8]

According to Yang *et al.*, the volume content of the hcp-transformed metal matrix in the alloy Stellite® 6 exhibits a proportional relationship to the SFE. This was found during isothermal aging experiments and traced back to changes in the chemical composition of the metal matrix due to the formation of Cr-rich carbides of the $M_{23}C_6$ type. Thereby, the precipitation of $M_{23}C_6$ carbides leads to a decrease of C and Cr in the metal matrix. Both elements are known to reduce the SFE in Co-base alloys.[9] However, for our work, we cannot rely on thermally induced carbide precipitation, as the working temperatures of tools for tunneling and mining rarely exceed 100 °C. While it would be possible to induce carbide precipitation during the production process by isothermal aging, the drawbacks of this procedure would likely outweigh the advantages: Apart from high costs due to long aging times at high temperature (> 100 hours at 700 °C), the carbide precipitation at grain boundaries and phase boundaries may cause unwanted embrittlement. Furthermore, the aging process would cause dissolution of the eutectic M_7C_3 carbides, which are generally wanted for their abrasion resistance.

Therefore, the SFE must be increased by alloy modification to stabilize the fcc phase at room temperature. Previous works have illustrated that Fe is particularly suitable to increase the SFE in Co-base alloys. Tisone experimentally determined the influence of partially substituting Co with Fe on the SFE of pure Cobalt by TEM investigations. At room temperature, he reported an SFE of ca. 25 mJ/m^2 at a Fe content of 8 at. pct (7.6 mass pct), compared to an SFE of $< 2\ mJ/m^2$ for pure Cobalt.[10] Achmad and coworkers validated these results by first-principles calculations and thermodynamic calculations. They calculated an SFE for the alloy system Co-8 at. pct-Fe in the range of 20 mJ/m^2 (thermodynamic calculations) to 30 mJ/m^2 (first-principles calculations). Furthermore, they reported an increase of the SFE with increasing Fe content up to 75 mJ/m^2 if a Fe content of 20 at. pct (19.15 mass pct) was present.[11,12]

Based on the illustrated state of literature, the following questions will be addressed in our work:

- How does the stacking fault energy (SFE) of Stellite® 6 correlate to the Fe content?
- Can we suppress the deformation-induced phase transition from α-Co (fcc) to ε-Co (hcp) at room temperature by a controlled increase of the SFE?
- Which amount of Fe must be added to stabilize the fcc phase in the Co-base metal matrix?
- How does the change of alloy composition affect the microstructure in terms of mechanical properties, carbide size, carbide morphology, and chemical composition of the carbides formed in Stellite® 6?
- Can we increase the fatigue limit of Fe-alloyed Stellite® 6 by suppressing the stress-induced fcc-hcp phase transition?

To answer these questions, we use four different laboratory heats of Stellite® 6, each with a different amount of substituted Fe content (0, 15, 25, 35 mass pct). The fatigue life of each specimen will be qualitatively determined to conclude the effectiveness of the alloy modification. Subsequently, the fatigue behavior is analyzed by SEM investigations of the microstructure and the crack paths that grow during the fatigue test. EBSD scans before the fatigue test and afterward are conducted to map the phase transition from fcc to hcp in the metal matrix of the specimens. XRD scans were carried out on additional heats with the chemical composition of the metal matrix to determine the influence of the change of the stacking fault energy at different Fe contents. In combination with a computational calculation of the formation enthalpy of the hcp phase, this enables us to analyze the influence of the stacking fault energy on the fatigue behavior of the Co-base alloys under investigation.

II. EXPERIMENTAL PROCEDURE

A. *Materials*

Four laboratory 200g heats of Stellite® 6 were cast in a vacuum furnace CM30 (Leybold-Heraeus, Germany) and cooled down in the furnace. Different amounts of Co were substituted by Fe, namely 0, 15, 25, and 35 mass pct. The chemical composition was determined by spark emission spectroscopy (QSG-750 II, OBLF) and is listed together with the nomenclature of the investigated specimens in Table I.

All alloys were investigated in as-cast conditions, without further heat treatment. Cubic specimens of width × length × height = 10 × 10 × 15 mm were cut from each melt for the cyclic loading test.

Four additional 200 g melts with the chemical composition of the metal matrix were cast in the same CM30 vacuum furnace. The composition for these melts was based on EDS scans of the metal matrix, which are listed in Table II. Due to the limited traceability of C by EDS, the carbon content was measured separately by wavelength dispersive X-ray analysis (WDX). The experimental procedure of the WDX scans is described in Section II–E.

These four melts were produced, as the experimental determination of the SFE of the Co-base metal matrix requires specimens of the pure metal matrix, without any hard phases present.

B. *Determination of the SFE*

In order to determine the SFE of the metal matrix of Stellite® 6 with 0, 15, 25, and 35 mass pct of substituted Fe, an experimental approach and a simulation-based route were used.

1. *Experimental methods*

For the experimental determination of the SFE, the X-ray diffraction (XRD)-based approach of Reed and Schramm[13] was chosen. According to their work, the SFE can be calculated by the following formula:

$$SFE = \frac{K_{111}\omega_0 G_{111} a_0}{\pi\sqrt{3}} \frac{<\varepsilon^2_{50\text{Å}}>}{\alpha} A^{-0.37}. \quad [1]$$

In this formula, K_{111} and ω_0 are lattice- and material-structure-dependent parameters, which were taken from the literature. G_{111} is the shear modulus of the (111)-plane, in which the stacking faults are formed, and a_0 is the lattice parameter of the fcc-metal matrix. The factor

$$\frac{<\varepsilon^2_{50\text{Å}}>}{\alpha}, \quad [2]$$

consists of the microstrain $\varepsilon_{50\text{Å}}$ of the (111) plane, divided by the stacking fault probability α, and is proportional to the SFE. The factor A is a fitting parameter, which compensates the elastic anisotropy of the material and allows a linear fit of the parameters K_{111} and ω_0 to the SFE.[13] The lattice parameter a_0 was experimentally determined for the dislocation-rich cold-worked (CW) state from the examined test alloys by XRD. The microstrain $\varepsilon_{50\ \text{Å}}$ was experimentally determined according to the approach of Popa *et al.*[14] In this approach, the microstrain is determined iteratively using the Rietveld method over the entire 2Θ-range and then the mean-square microstrain $<\varepsilon^2_{50\text{Å}}>$ of the (111) reflection is calculated. The microstrain can be analyzed from the full width at half maximum (FWHM) of the (111)-reflection positions (see Figure 1(a)) and is used to determine the SFE.

According to Popa,[14,15] the stacking fault probability α can be calculated as the difference in distance of the (111) and (200)-reflex positions, because stacking faults cause a shift of the (200) reflex and this shift correlates with the amount of stacking faults present. For this approach, a dislocation-rich cold-worked (cw) state and a dislocation-free annealed (ann) state (see Figure 1(b)) are necessary and the stacking fault probability α can be calculated by the formula:

$$\begin{aligned}\Delta 2\Theta &= (2\Theta_{200} - 2\Theta_{111})_{CW} - (2\Theta_{200} - 2\Theta_{111})_{ANN} \\ &= -\frac{45\sqrt{3}}{\pi^2}\alpha[\tan\Theta_{200} - 0.5\tan\Theta_{111}]_{ANN}. \end{aligned} \quad [3]$$

For the XRD measurements, a total of 2 g chips, produced by filing material from the solid cast specimen, was acquired from each casting of the metal matrix compositions to obtain material in a cold-worked state (cw). Half of the file chips were afterwards encapsulated under vacuum, annealed at 1210 °C for 30 minutes, and quenched in water to create a dislocation-free fcc-metal matrix (ann). The annealing temperature of 1210 °C was chosen to avoid the formation of M_7C_3 carbides, which form below this temperature. This type of carbide precipitation had to be avoided, in order to not compromise the XRD measurements. Both species (cw and ann) were separately positioned on a specimen holder and installed in the diffractometer.

Table I. Chemical Composition of the Stellite® 6 Specimens With Partial Fe Substitution in Mass Percent

Specimen	Fe	Cr	W	C	Si	Co
S6-0Fe						
Nominal composition	> 0.5	28.00	4.50	1.60	0.70	bal.
Measured composition	0.44	28.64	4.00	1.86	0.91	bal.
S6-15Fe						
Nominal composition	15.00	28.00	4.50	1.60	0.70	bal.
Measured composition	15.73	28.36	4.31	1.79	0.83	bal.
S6-25Fe						
Nominal composition	25.00	28.00	4.50	1.60	0.70	bal.
Measured composition	25.43	28.18	4.28	1.73	0.85	bal.
S6-35Fe						
Nominal composition	35.00	28.00	4.50	1.60	0.70	bal.
Measured composition	35.61	28.60	4.12	1.82	0.79	bal.

A D8 Advance diffractometer of the company Bruker was used for all XRD measurements in a Bragg–Brentano arrangement. Cu-K_α radiation ($\lambda_{Cu\text{-}K\alpha1} = 0.154060$ nm, $\lambda CuK\alpha2 = 0.154439$ nm) was used and a nickel filter suppressed Cu-K_β radiation. An acceleration voltage of 40 kV and a working current of 40 mA were used in all experiments. The investigated 2Θ angles ranged from 25 to 100 °2Θ, using a step width of 0.005 °2Θ at an acquisition time of 2 seconds for each step. The results of the XRD measurements were analyzed by means of a Rietveld refinement using the software MAUD.[16]

2. *Computational methods*

The simulation-based approach to determine the SFE uses the method of Olson and Cohen,[17] who proposed the formula:

$$SFE = n\rho_A\left(\Delta G^{fcc\rightarrow hcp} + E^{str}\right) + 2\sigma_s, \quad [4]$$

for the calculation of the SFE. In this formula, n is the number of atomic planes involved in forming a stacking fault, ρ_A is the surface density, and σ_S is the interfacial energy between the fcc and hcp phase.[17] The surface density ρ_A was calculated by the formula:

$$\rho_A = \sqrt[3]{\frac{1}{V_m^2 N_0}}, \quad [5]$$

where V_m is the molar volume of the standard unit cell of the material and N_0 is the Avogadro constant. As the contribution of the strain energy E^{str} is usually small (< 0.1 pct of the SFE), it will be neglected in the calculation.

The parameter ΔG^{fcchcp} was determined by calculating the free enthalpy difference between the fcc and hcp phases for the known chemical composition, using the software ThermoCalc, version 2022a. The TCNI10 database was used for all calculations, as a previous version of this database had already been used successfully by Tian *et al.*[8] for Co-Fe alloys. An ambient temperature of 294.5 K and a pressure of 1×10^5 Pa were assumed. For the thermodynamic calculation of the Gibbs energy of the fcc and hcp phase, all other phases were suspended and the global minimization deactivated.

The required value σ_S for the interfacial energy was backward calculated by inserting the experimentally determined SFE of the specimen S6-35Fe_matrix into Eq. [4] and solving for σ_S.

C. *Hardness Measurements*

The macrohardness of the specimens was determined according to DIN EN ISO 6507 with the hardness tester KB 30 (KB Prüftechnik, Germany), using a load of 294,2 N (HV30). In addition, the microhardness of the metal matrices and the hard phases was determined phase resolved by instrumented indentation testing with a nanoindenter NHT (CSM instruments, Switzerland) following DIN EN ISO 14577-1. A Berkovich indenter was used, and the target load of 50 mN and a maximum indentation depth of 5 μm were applied. Load–indentation curves were analyzed based on Oliver and Pharr method.[18,19] The indentation hardness was calculated using a Poisson ratio of 0.3 for the CoCrW metal matrix and 0.27 for the M_7C_3 hard phases, based on literature values.[20–22] Due to the various chemical compositions of the M_7C_3 carbide, an interpolated value between the values stated by Casellas[21] and Xiao[22] was chosen.

D. *Cyclic Load Testing*

Before the cubic-shaped specimens were positioned into the testing machine, their top surface was ground with SiC grinding paper (1000 mesh) and polished with 1 μm diamond suspension to ensure equal surface quality of all specimens. The cyclic load testing was subsequently conducted in an electrodynamic testing machine Electropuls E3000 (Instron, United Kingdom). A spherical Si_3N_4 Indenter applies the load with a diameter of 10 mm (hardness = 1500 HV0.05) in the form of sinusoidal pulsating thrusts with a maximum load of 2800 N in the compressive regime and with a frequency of 25 Hz. A schematic illustration of this setup is shown in Figure 2. The indenter is constantly in contact with the specimen surface due to a pre-force of 50 N, applied by two tension springs.

The tests were continued until either fracture of the specimens occurred in the form of a ring crack around the contact area between specimen and indenter, or until a total number of 1.5×10^8 load cycles was reached. To assess the progress of the crack growth, the fatigue tests were interrupted several times for light-microscopic investigations. For this purpose, a microscope of type Olympus BX60 (Zeiss, Germany) was used. The specimens were not ground or polished before the light-microscopic examinations to keep the condition of the tribological system as intact as possible.

E. *Metallography and Microscopy*

After finishing the fatigue test, the cyclically loaded specimens were prepared for SEM examinations by polishing with 1 μm diamond suspension for approximately 1 minute to remove oxide layers and debris from the surface to be investigated. They were then vibro-polished with 0.05 μm oxide suspension for 12 hours, ensuring high pattern quality of subsequent EBSD scans.

An SEM of the type Mira 3GM (TESCAN, Germany) was used to acquire images of the specimens' microstructure. The backscattered electron (BSE) detector was used at a working distance of 10 mm and an acceleration voltage of 18 kV. The Xman detector and the evaluation software AZtec (Oxford Instruments, United Kingdom) were employed for EDS Scans to determine the chemical composition of the metal matrix and the hard phases. The acceleration voltage and the working distance were changed to 25 kV and 15 mm. Determination of the carbon content in the metal matrix of the alloys was carried out separately by the means of wavelength dispersive X-ray analysis (WDX), using the WAVE detector (Oxford Instruments, United

Table II. Chemical Composition of the Metal Matrices of the Stellite® 6 + Fe Specimens, Measured by EDS Scans, Except for Carbon. Carbon was Measured Separately by WDX Scans. All Values in Mass Percent

Specimen	Fe	Cr	W	C	Mn	Si	Ni	Co
S6-0Fe_matrix	0.6	23.6	4.5	0.156	0.5	0.7	1.8	bal.
S6-15Fe_matrix	16.0	23.8	4.8	0.240	0.4	0.5	2.0	bal.
S6-25Fe_matrix	26.3	22.9	4.3	0.125	0.4	0.8	1.5	bal.
S6-35Fe_matrix	36.8	23.5	4.2	0.215	0.4	0.8	1.5	bal.

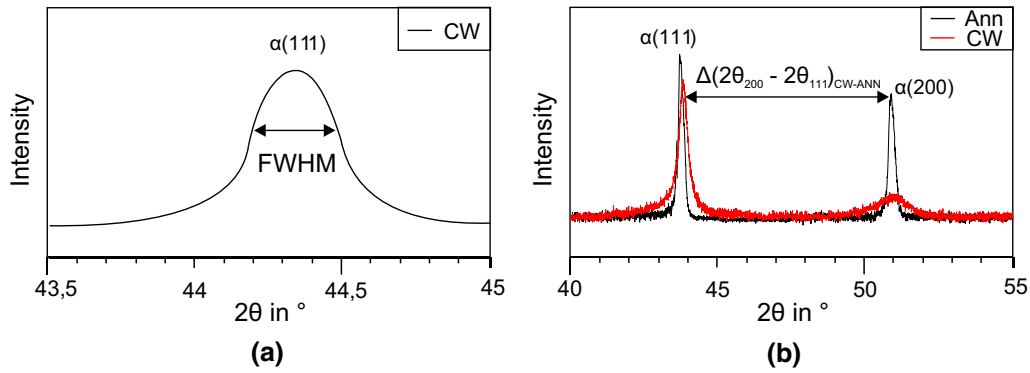

Fig. 1—Determination of the required parameters for the approach according to Reed and Schramm by means of the XRD measurements. (*a*) The microstrain ε was determined by measurement of the full width of the α-Co (111) reflection at half of the height of the maximum (FWHM). (*b*) The stacking fault probability of α-Co was measured from the difference in distance between the α(111) and α(200) reflection in the annealed (ann) and cold-worked (cw) condition.

Kingdom). For these measurements, the specimens were embedded in carbon-free embedding material and prepared together with two reference samples. This way, the effect of possible carbon contamination during preparation can be reduced. Pure iron (carbon content 0.001 mass pct) and a sample of the austenitic X120MnCr12 steel (carbon content 1.241 mass pct) were used as reference standards to allow for a large measurement range. The carbon content of the reference samples was determined by carrier gas hot extraction on a CS-800 analyzer (ELTRA, Germany). Prior to measurement, the specimens and the SEM chamber were plasma cleaned for 20 minutes and the cooling probe of the SEM was filled with liquid nitrogen to ensure high vacuum quality. The acceleration voltage was set to 5 kV. For carbon measurements, the layered synthetic crystal LSM80N with an atomic layer distance of 78 Å was employed. The beam current was measured and normalized every 5 minutes during the WDX measurements. Five-point measurements were conducted for each specimen and each reference sample. Data acquisition and processing were carried out by the software INCA Wave® (Oxford Instruments, United Kingdom). A linear fit line was calculated for the reference samples, and the carbon content of the investigated specimens was calculated based on interpolation on the fit line.

EBSD Scans were conducted, using the Nordlys Nano Detector (Oxford Instruments, United Kingdom) and the AZtec software. The specimens were tilted by an angle of 70 deg for the EBSD scans. The inorganic crystal structure database (ICSD) was used for the

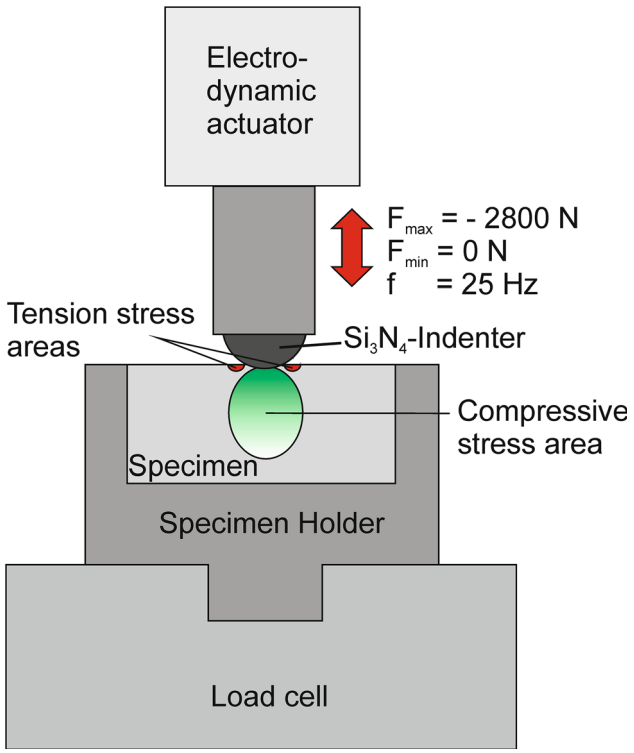

Fig. 2—Schematic illustration of the cyclic compressive test setup and visualization of the stress distribution in the specimen, below and outside of the contact area to the indenter.

identification of the phases α-Co, ε-Co, Cr_7C_3, and $(Cr, W)_{23}C_6$. For the analysis of crystallographic directions and the segmentation of inverse pole figure images, the software HKL Channel 5 (Oxford Instruments) was used. The subprogram Tango was used for segmentation of inverse pole figure images, and the subprogram Mambo was used for measurement of crystallographic relationships and misorientation angles.

To determine the mean volume content V_{HP} and size of the hard phases d_{HP} in the specimens, five SEM images of the microstructure of each specimen were binarized with the software ImageJ (Fiji distribution), and the respective parameters are calculated as the average from the particle analysis of the five images. In addition, the mean-free matrix path λ_{MM} was determined with the linear intersect method, using the software A4i-Analysis (Aquinto, Germany). A confocal laser-scanning microscope VK-X200 (Keyence, Japan) was utilized for the acquisition of surface profiles after fatigue testing. The diameter and depth of the calotte-shaped indent in each specimen were measured at five positions and the results were averaged.

III. RESULTS AND DISCUSSION

A. *Stacking Fault Energy*

To measure the SFE of the metal matrices in the various specimens, XRD scans were conducted on file chips of the matrix material in the cold-worked (cw) and annealed (ann) condition. Figure 3 shows the patterns between the range of the angles 40 and 55 deg 2Θ, which includes the positions of the α(111) and α(200) reflections of the Co-matrix phase that is necessary for the calculation of the SFE. In the annealed state, the α(111) and α(200) reflections are present for each specimen, proving the single α-Co phase state of these alloys. Furthermore, no ε-Co reflections were detected; thus, the matrix exclusively consists of the α-Co phase.

The XRD patterns of the file chips in cold-worked (cw) condition of specimens S6-0Fe_matrix and S6-15Fe_matrix only contain ε-Co reflections, indicating that a severe plastic deformation during the file-chip production caused a complete phase transformation of the metal matrix from α-Co (fcc) to ε-Co (hcp) for these two alloy compositions. In the cold-worked state, α-Co reflection positions could only be indicated for the specimens containing 25 or 35 substituted mass pct-Fe, respectively. Also, for the sample having 35 mass pct substituted Fe, no ε-Co reflections were detected, indicating a stable α-Co metal matrix after severe plastic deformation. The results of the quantitative phase analysis using the Rietveld method are listed in Table III.

Based on the results of the XRD experiments and materials constants from the literature (Table IV), the SFE of the metal matrix in specimen S6-35Fe was calculated to 35 mJ/m^2. It was, however, not possible to experimentally determine the SFE for the other three specimens, since the Reed and Schramm approach can only be applied to stable fcc systems.

Due to the complete phase transition from α-Co to ε-Co in the metal matrix of the specimens S6-0Fe_matrix and S6-15Fe_matrix, the positions of the α(111) and α(200) reflections could not be determined for the cold-worked condition. Therefore, it was not possible to measure the SFE experimentally. Several previous works[10,24] indicate that the SFE of the metal matrix of Co-base alloys is below 20 mJ/m^2. For CoCrMo alloys, negative SFEs have already been reported by Mitsunobo.[25] The possibility and significance of such negative SFEs are debated in the literature, as they cannot be measured with experimental SFE-measurement techniques due to limitations of the available methods and due to simplifications in the known experimental approaches.[26,27] Sun[28] proposed that negative SFEs may give a more suitable explanation for the deformation mechanisms of metastable alloys, which applies to Stellite 6® and other CoCrWC-alloys. It was also suggested that for metastable alloys, the Gibbs energy difference between fcc and hcp phase, $\Delta G^{fcc \rightarrow hcp}$, gives a better correlation to the material behavior than experimentally determined SFEs [28]. For this reason, we used thermodynamic calculations to determine $\Delta G^{fcc \rightarrow hcp}$ for the different alloy compositions.

The values of $\Delta G^{fcc \rightarrow hcp}$, as well as the molar volume V_m, and the interfacial energy σ_S, were calculated according to the procedure described in Section II.B. The results of the calculations are listed in Table V. The Gibbs energy difference generally increases with the iron content, from negative values for the specimens S6-0Fe_matrix (− 1195 J/mol), S6-15Fe_matrix (− 373 J/mol), and S6-25Fe_matrix (− 517 J/mol) to a positive value for the specimen S6-35Fe_matrix (226 J/mol). These results show a good correlation to the findings of the XRD experiments, as they confirm the stability of the fcc α-Co for iron contents of 35 mass pct and above, as well as the phase transformation into hcp ε-Co at lower iron contents.

The Gibbs energy difference of specimen S6-25Fe_matrix does not entirely fit the general trend, which may be explained by small differences in the chemical composition, compared to the other specimens.

The molar volume V_m slightly increases with the iron content, due to the larger atomic radius of iron compared to cobalt, from 6.964×10^{-6} m^3/mol in specimen S6-0Fe_matrix to 7.010×10^{-6} m^3/mol in specimen S6-35Fe_matrix.

We inserted the experimentally determined SFE of the specimen S6-35Fe into formula [4] to obtain a value for the interfacial energy σ_S between α_{Co} and ε_{Co}, which is necessary for the SFE calculation according to the approach of Olsen and Cohen. The calculated value of 10.2 mJ/m^2 was used to determine the SFE of the specimens S6-0Fe_matrix, S6-15Fe_matrix, and S6-25Fe_matrix, which could not be determined experimentally. We are aware that the interfacial energy is influenced by the chemical composition, and that therefore, the calculated SFE values will contain a small error. However, due to the linear character of σ_S in formula [4], this error will not change the qualitative findings regarding the SFE.

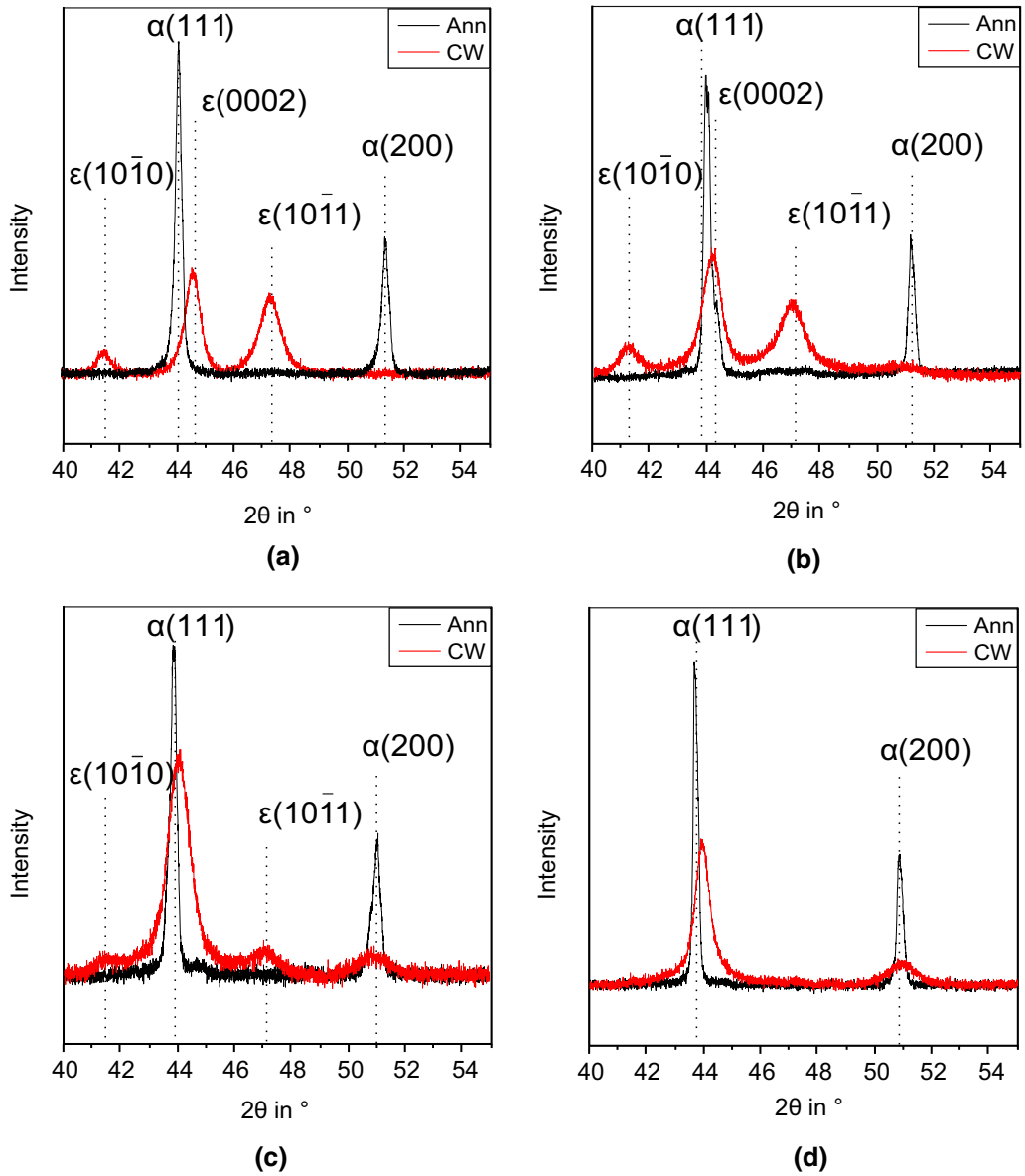

Fig. 3—Excerpts of the XRD scans on file chips of the investigated specimens in annealed (ann) and cold-worked (cw) conditions. The range of the 40 to 55 deg 2Θ angles was chosen, as it includes the reflex positions α(111) and α(200), which are necessary for the SFE-determination according to the method of Reed & Schramm. (*a*) S6-0Fe_matrix, (*b*) S6-15Fe_matrix, (*c*) S6-25Fe_matrix, (*d*) S6-35Fe_matrix.

Table III. Phase Contents Determined by Quantitative Phase Analysis Using the Rietveld Method in MAUD of the File Chips

Specimen	Condition	α-Co (Vol Pct)	ε-Co (Vol Pct)
S6-0Fe_matrix	ann	100	0
S6-0Fe_matrix	cw	0	100
S6-15Fe_matrix	ann	100	0
S6-15Fe_matrix	cw	0	100
S6-25Fe_matrix	ann	100	0
S6-25Fe_matrix	cw	26.1	73.9
S6-35Fe_matrix	ann	100	0
S6-35Fe_matrix	cw	100	0

The calculated SFE of the metal matrix in the specimens S6-0Fe_matrix, S6-15Fe_matrix, and S6-25Fe_matrix is negative, which fits the experimental observation of a complete phase transformation of the metal matrix during plastic deformation. The lowest SFE of $-57\ mJ/m^2$ was calculated for specimen S6-0Fe_matrix, with the lowest iron content. Due to the more negative Gibbs energy difference, the SFE of specimen S6-25Fe_matrix ($-13\ mJ/m^2$) is lower than the SFE of specimen S6-15Fe_matrix ($-4\ mJ/m^2$).

Table IV. Collection of the Input Parameters for the SFE-Calculation of Specimen S6-35Fe_Matrix and Calculated SFE, as Well as Backward Calculated Interfacial Energy σ_S

Property	Value in SI Units	Source
K_{111}	28 [–]	[13]
$\omega 0$	0.1666667 [–]	[13]
G_{111}	0.65 N/m^2	[23]
A	3.34 [–]	[23]
a_0	3.595 Å	XRD measurement
ε	4.8×10^{-6} [–]	XRD measurement
$2\Theta_{111}$ ann	43.69 deg	XRD measurement
$2\Theta_{111}$ cw	43.95 deg	XRD measurement
$2\Theta_{200}$ ann	50.85 deg	XRD measurement
$2\Theta_{200}$ cw	50.94 deg	XRD measurement
α	0.0844	calculation
SFE	35 mJ/m^2	calculation
σ_S	10.2 mJ/m^2	calculation

B. *Microstructure and Mechanical Properties of the Specimens Before Cyclic Loading*

The microstructure of each specimen was investigated prior to the fatigue testing to determine any differences in the microstructure due to the partial substitution of Co with Fe. SEM images of the microstructures of the respective specimens are shown in Figure 4 and values for the hard phase content V_{HP}, mean hard phase size d_{HP}, and the mean-free matrix path λ_{MM} are listed in Table VI. In the context of the present alloys, λ_{MM} corresponds to the mean size of the primary metal matrix cells.

All specimens show a hypoeutectic microstructure, consisting of primary cells of the metal matrix and eutectic carbides. The carbides are distributed in a eutectic-shaped morphology but do not form a continuous network. EBSD scans (Figure 5) reveal that the carbides are mainly of the type M_7C_3, aside from a smaller amount of M_6C carbides. While the carbide content of all specimens is in the range of 13 to16 vol pct, the content of the M_6C carbides increases with the substituted amount of Fe from < 0.5 vol pct in the specimen S6-0Fe up to 3.2 vol pct in the specimen S6-35Fe. The determined carbide content is in good agreement with the values of 14.5 vol pct experimentally measured by Yang *et al.*, as well as by Krell *et al.* (15.0 vol pct) for cast Stellite® 6 alloys.[1,9] The mean carbide diameter is similar at about 3.5 to 5.5 μm for all specimens. The metal matrix of all specimens has a fcc lattice structure (> 95 vol pct) with only small amounts of hcp phase, which are mainly located adjacent to carbides (Figures 5(a) through (c)). The size of the primary metal matrix cells (λ_{MM}) ranges from 11.68 ± 2.50 μm in specimen S6-15Fe to 13.17 ± 2.34 μm in specimen S6-0Fe.

From this comparison of the microstructural parameters, it can be derived that the substitution up to 35 mass pct Co with Fe did not affect the microstructure of the alloy in such a manner that it could cause a significantly different fatigue behavior.

To determine differences in the mechanical properties, the hardness of the specimens was measured macroscopically and phase resolved for the metal matrix and the hard phases. Table VII lists the results of these hardness measurements. The macroscopic hardness of the specimens decreases about 10 pct with increasing Fe content, from 423 HV30 in specimen S6-0Fe to 382 HV30 in specimen S6-35Fe. The results of the nanoindentation experiments show that the decrease in hardness is caused by softening of the metal matrix with increasing Fe content: Without substituted Fe, the indentation hardness of the Stellite® 6 metal matrix was measured to 5.17 GPa, compared to a hardness of 4.58 GPa in the specimen with 35 mass pct substituted Fe. One reason for reducing the metal matrix hardness is the lowered amount of the harder ε-Co phase at higher Fe contents, due to the increasing stability of the α-Co phase with higher iron contents.

The hardness of the M_7C_3 carbides exhibits no clear tendency towards lower hardness with increasing iron content but fluctuates between 15.93 ± 1.04 GPa in sample S6-15Fe and 16.62 ± 0.60 GPa, measured in sample S6-0Fe. The results of EDS point scans (Table VIII) reveal that with increasing Fe content in the alloy composition, the Fe content in the carbides increases from 0.7 at. pct in specimen S6-0Fe to 12.5 at. pct in specimen S6-35Fe. Simultaneously, the Cr content in the carbides is reduced, which is commonly associated with a loss of hardness.[4] However, no severe drop in the hardness of the M_7C_3 carbides was measured with increasing Fe content. This can be attributed to the reduction of the Co-content in the carbides, which drops from 8.89 at.pct in specimen S6-0Fe to 1.3 at.pct in specimen S6-35Fe and is mainly replaced by Fe.

C. *Fatigue Behavior*

Fatigue testing caused the formation of a calotte-shaped indent in the specimen surface. The diameter and depth of the indents are listed in Table IX. The diameter of the indent increases with the iron content about 2.6 pct from 1618 μm at specimen S6-0Fe to 1660 μm at specimen S6-35Fe. The depth of the indent, relative to the highest point of the plasticity induced embankment at the outside of the indent, is also lowest for specimen S6-0Fe at 26.8 μm. The largest indent depth was measured for specimen S6-25Fe at about 31.4 μm. These results indicate that the strength of the specimens slightly decreases with the iron content, as they experienced more plastic deformation due to fatigue testing. It should, however, also be noted that the number of load cycles was increased with the iron content, which resulted in an overall higher amount of loading placed on these specimens.

The fatigue behavior of the various specimens was determined by analyzing the microstructure of the specimens around the contact area to the indenter. Special emphasis was put on the crack paths and the interaction of the crack with the microstructure constituents metal matrix, hard phases, and interfaces between metal matrix and hard phases. Figure 6 shows

Table V. Results of the Computational Calculations of the Gibbs Energy for hcp Phase in the fcc Metal Matrix of the Investigated Specimens, as well as Calculated Molar Volume and SFE

Specimen	Gibbs Energy of ε_{Co} (J/mol)	Gibbs Energy of α_{Co} (J/mol)	ΔG^{fcchcp} (J/mol)	Molar Volume V_m (10^{-6} m^3/mol)	Calculated SFE (mJ/m^2)
S6-0Fe_matrix	− 9999	− 8804	− 1195	6.966	− 57
6-15Fe_matrix	− 10140	− 9767	− 373	6.998	− 4
S6-25Fe_matrix	− 0025	− 9508	− 517	7.034	− 13
S6-35Fe_matrix	− 8698	− 8924	226	7.010	(35)

The SFE of Specimen S6-35Fe_matrix was Determined Experimentally and was Used for Backwards Calculation Purposes.

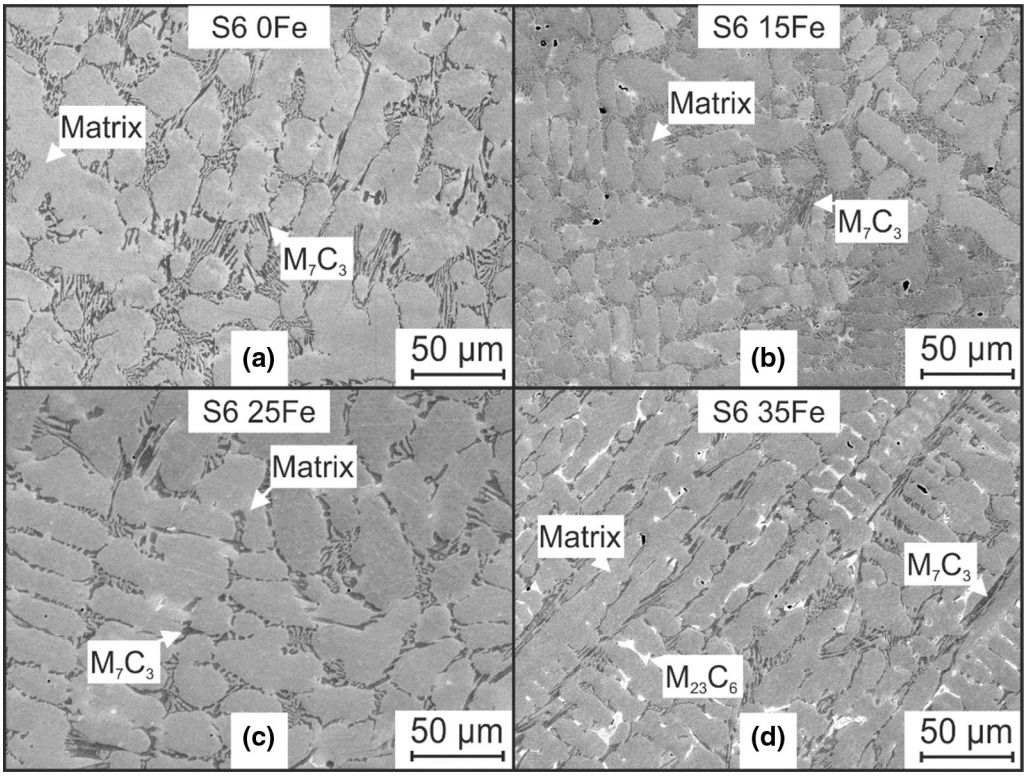

Fig. 4—Representative excerpts of the microstructure before fatigue testing for the specimens: (*a*) S6-0Fe, (*b*) S6-15Fe, (*c*) S6-25Fe, (*d*) S6-35Fe.

Table VI. Microstructural Parameters of the Various Stellite® 6 + Fe Specimens

Specimen	V_{HP} (Vol. Pct)	λ_{MM} (μm)	d_{HP} (μm)
S6-0Fe	16.19 ± 2.15	13.17 ± 2.34	5.48 ± 1.27
S6-15Fe	15.67 ± 1.19	11.68 ± 2.50	3.40 ± 0.81
S6-25Fe	13.75 ± 0.38	12.59 ± 1.87	3.64 ± 1.19
S6-35Fe	14.22 ± 0.94	12.34 ± 2.45	4.71 ± 1.02

representative excerpts of the microstructures after fatigue testing for each specimen.

The crack path in specimen S6-0Fe (Figure 6(a)) is characterized by straight-lined crack growth, primarily inside the metal matrix. Fracture of the hard phases or debonding of the hard phases from the metal matrix is only observed if the hard phases represent obstacles to the crack path. Several parallel side cracks to the continuous main crack are visible in multiple metal matrix cells. These side cracks end at the grain boundary of the respective metal matrix cell which indicate that the metal matrix has a higher local susceptibility to fatigue crack propagation compared to the interdendritic regions.

As the width of the cracks is very narrow, the macroscopic crack path is schematically visualized by the drawing in Figure 7(a), and additional SEM images (Figures 7(b) and (c)) of the crack propagation through multiple grains are presented. The macroscopic crack path deviates from a perfectly circular shape, which would have been expected based on the circular shape of the prevailing tensional stress field around the contact area created by the spherical indenter. Instead, the crack path diverges away from the contact area on multiple locations, as there are hardly any changes in the crack growth direction in the metal matrix. This indicates a

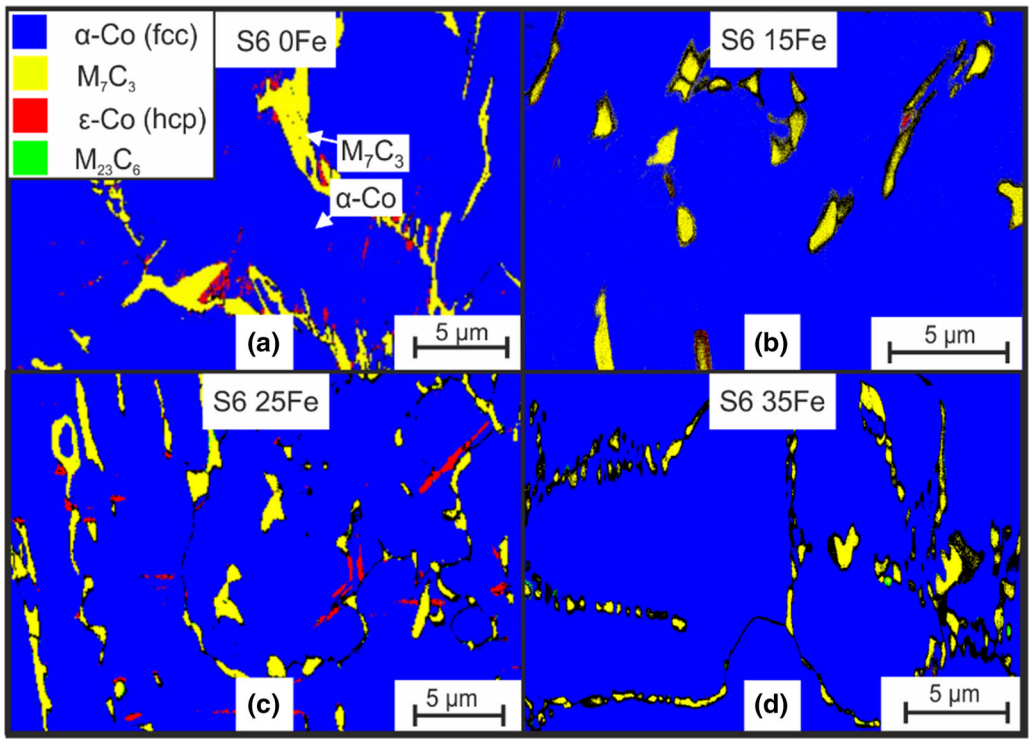

Fig. 5—EBSD scans of the investigated specimens prior to fatigue testing: (*a*) S6-0Fe (*b*) S6-15Fe (*c*) S6-25Fe (*d*) S6-35Fe.

strong dependency of the crack propagation on the microstructure in general, and in particular, on directional properties of the metal matrix. After 4.5×10^7 load cycles, a fully developed ring crack was formed in specimen S6-0Fe. A previous SEM observation at 1.5×10^7 load cycles already revealed crack growth, which bridged several grains (Figure 6(b)). It is, therefore, assumed that the initiation of first cracks occurred significantly earlier.

Specimen S6-15Fe (Figure 6(c)) exhibits a fatigue behavior similar to the one observed in specimen S6-0Fe, with predominant fracture of the metal matrix and almost no crack growth through the hard phases or through the interfaces between hard phases and metal matrix. A fully developed ring crack was observed at 8×10^7 load cycles for this specimen. At the lifetime of 4.5×107 load cycles, at which the specimen with no Fe addition had formed a ring crack, this specimen only showed short cracks inside the metal matrix (Figure 6(d)).

A first change in the fatigue behavior of the Stellite® 6 alloy can be observed at a substituted Fe content of 25 mass pct. The crack path in specimen S6-25Fe (Figure 6(e)) is no longer limited to the metal matrix but shifted towards fracture of the hard phases. As a result, this specimen shows crack retardation instead of the straight-lined crack growth in the previously discussed specimens with a lower Fe content. Specimen S6-25Fe formed no closed ring crack until the termination criterion at 1.5×10^8 load cycles; however, due to the length of the existing cracks (> 250 μm), it can be assumed that this specimen would form a closed ring crack at a higher number of load cycles. At 1×10^8 load cycles, microcracks had been observed at fractured hard phases, which had not yet crossed a metal matrix cell (Figure 6(f)). As the cracks only grew to a size of about 250 μm in the following 5×10^7 load cycles, the crack velocity is very low. This can be attributed to the behavior of the metal matrix, which showed a significantly improved crack growth resistance.

The fatigue behavior of specimen S6-35Fe is most different compared to the other specimens. At the termination of the fatigue test at 1.5×10^8 load cycles, no crack growth in the metal matrix of this specimen could be observed. Only small cracks were found at the necks of hard phases, which are most susceptible to fracture (Figure 6(h)). While it is possible that the hard phase fracture occurred after a very high number of load cycles, it appears more likely that the cracks that were initiated by hard phase fracture were stopped entirely by the surrounding metal matrix.

EBSD scans were conducted on all specimens after fatigue testing to reveal the relationships between the crystallographic orientation of the grains, phase transformations, and the crack path. Figure 8 shows excerpts of the local phase distribution in the microstructure of the specimens after fatigue testing. In the specimens S6-0Fe, S6-15Fe, and S6-25Fe, significant amounts of ε-Co were formed due to a local deformation-induced phase transformation of the former fcc metal matrix. The ε-Co mainly has a lath-shaped morphology and one end of the ε-Co laths is usually located at the interface of the metal matrix to a hard phase. This behavior can be attributed to the microstructural response of the material in the case of external loading. The metal matrix has a much higher plastic deformation capability compared

Table VII. Results of the Macrohardness and Phase-Resolved Microhardness Measurements

Specimen	Macrohardness (HV30)	Indentation Hardness of the Metal Matrix (GPa)	Indentation Hardness of the M_7C_3 Carbides (GPa)
S6-0Fe	423 ± 3	5.17 ± 0.36	16.62 ± 0.60
S6-15Fe	397 ± 3	4.93 ± 0.20	15.93 ± 1.04
S6-25Fe	388 ± 2	4.84 ± 0.58	16.27 ± 0.45
S6-35Fe	382 ± 3	4.58 ± 0.32	16.41 ± 0.72

Table VIII. Chemical Composition of the M_7C_3 Hard Phases of the Stellite® 6 + Fe Specimens, Measured by EDS Scans

Specimen	Fe	Cr	W	Co
S6-0Fe	0.7	52.5	4.5	8.9
S6-15Fe	3.6	50.1	5.7	6.3
S6-25Fe	5.8	49.6	6.4	4.4
S6-35Fe	12.5	47.6	4.2	1.3

All values in at pct. Due to the limited traceability of C by EDS, the values of C are not stated.

Table IX. Diameter and Depth of the Calotte-Shaped Indent in Each of the Specimens After Fatigue Testing

Specimen	Indent diameter (μm)	Indent depth (μm)
S6-0Fe	1618.54 ± 16.92	26.81 ± 1.84
S6-15Fe	1626.37 ± 28.45	28.13 ± 2.27
S6-25Fe	1621.02 ± 54.99	31.39 ± 1.10
S6-35Fe	1660.87 ± 24.30	29.07 ± 2.36

to the hard phases if external loads are applied. Therefore, the resulting strains accumulate at the hard phases and cause accommodation stresses. These accommodation stresses help overcome the activation barrier for the α-Co to ε-Co phase transformation, and therefore, ε-Co laths are preferentially formed at the interface between hard phases and metal matrix. It is observed that the ε-Co laths are either parallel to each other, or enclose an angle of about 56 deg. This can be attributed to the orientation relation between the fcc and the hcp phases, which are described by the Shoji-Nichiyama relation $(111)_{FCC}//(0001)_{HCP}$ and $\langle 110\rangle_{FCC}//\langle 11\bar{2}0\rangle_{HCP}$.[29] The validity of this orientation relationship was proven on the example of specimen S6-25Fe by computational comparison of the crystallographic directions of the fcc phase and the adjacent hcp phase (Figure 9(b)). White interface lines in this image indicate a misorientation angle of < 10 deg from the ideal orientation of fcc and hcp areas, which applies to almost every interface.

Figures 8(a) through (c)) illustrate that the crack path in the specimens that show the ε-Co phase transformation coincides with location of the ε-Co laths. It is, therefore, assumed that the phase transformation from α-Co to ε-Co facilitates crack growth, as ε-Co has a reduced number of slip systems compared to α-Co and, thus, causes local embrittlement of the metal matrix.

The crystallographic directions of the individual grains are illustrated in Figures 9(c) through (f) by the means of segmented inverse pole figures (IPFs). It is visible that some ε-Co grains are oriented with their basal (0001)-plane parallel to the surface (red areas in Figure 9(c)), and others with their $(\bar{1}2\bar{1}0)$-prism plane almost parallel to the surface (green areas in

Figure 9(c)). The misorientation angle from a perfectly parallel orientation of the $(\bar{1}2\bar{1}0)$-planes to the surface was measured to 17 deg. The crack path is exclusively located in the ε-Co grains that are almost parallel to the surface with their $(\bar{1}2\bar{1}0)$-prism plane.

For further information about the crack growth inside the volume of the material, an EBSD Scan was performed on a crack in the previously cut and 90 deg tilted specimen S6-15 Fe (Figure 10). Due to the close proximity to the contact area to the indenter and the largely transformed metal matrix, the amount of unindexed data points increases towards the specimen surface. The crack encloses a 45 deg angle to the surface, which is characteristic for the slip of (111) planes in fcc phases.

As the surrounding metal metal matrix is, however, completely transformed to ε-Co, the slip of (111)-fcc planes could have only occurred before the phase transformation. Another observation is that the crack is located in ε-Co laths with a different orientation, compared to the surrounding ε-Co metal matrix, which are located at a 45 deg angle to the specimen surface as well (Figures 10(c) and (d)). This indicates that the transformation of the metal matrix from α-Co to ε-Co does not occur simultaneously for all areas but rather in an iterative process: First, single ε-Co laths are formed at the locations of (111)-planes with a 45 deg angle to the surface. These ε-Co laths also represent the nucleation points for the crack initiation in the metal matrix. In the following, the remaining α-Co metal matrix is transformed to ε-Co as well but does not take part in the path of the crack growth. From the previously described mechanism, it becomes apparent that the phase transformation from α-Co to ε-Co causes a local deterioration of the metal matrix in Stellite® 6, which causes crack initiation and propagation and, therefore, represents the limiting factor for the fatigue life under cyclic loading.

The phase transformation from α-Co to ε-Co was observed in all specimens with an iron content of

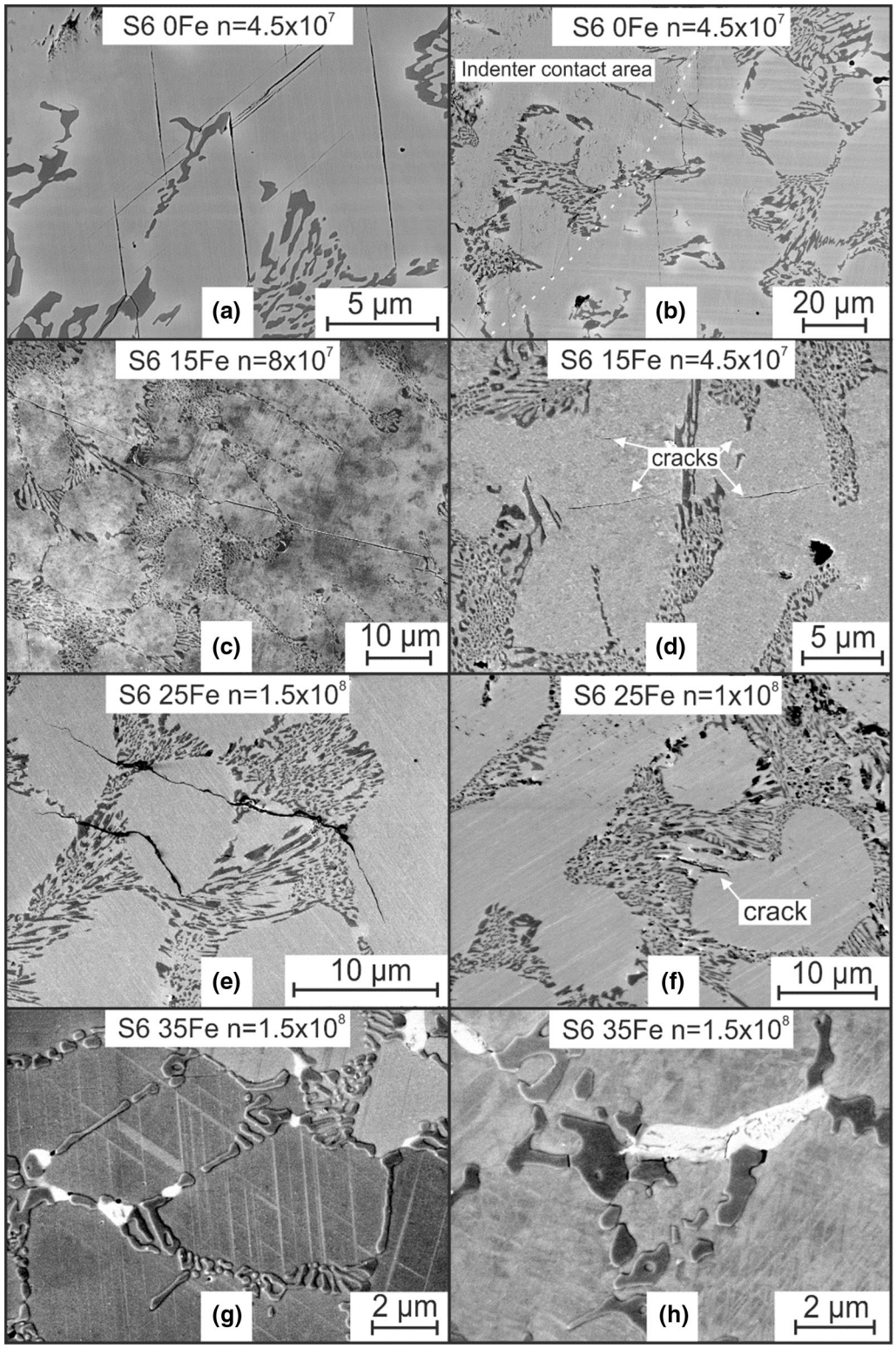

Fig. 6—Representative excerpts of the microstructure for each specimen after fatigue testing: (*a*) S6-0Fe at termination of the fatigue test at 4.5×10^7 cycles, (*b*) S6-0Fe at 1.5×10^7 cycles, (*c*) S6-15Fe at termination of the fatigue test at 8×10^7 cycles, (*d*) S6-15Fe at 4.5×10^7 cycles, (*e*) S6-25Fe at termination of the fatigue test at 1.5×10^8 cycles, (*f*) S6-25Fe at 1×10^8 cycles, (*g*) S6-35Fe at termination of the fatigue test at 1.5×10^8 cycles, and (*h*) S6-35Fe at termination of the fatigue test at 1.5×10^8 cycles.

25 mass pct and below. At the same time, the SFE of the metal matrix of these specimens was calculated to be negative, which is indicative of the observed metastable behavior. The specimen S6-35Fe with a positive SFE of 35 mJ/m^2 did not perform a phase transformation of the metal matrix. Instead, a shift of

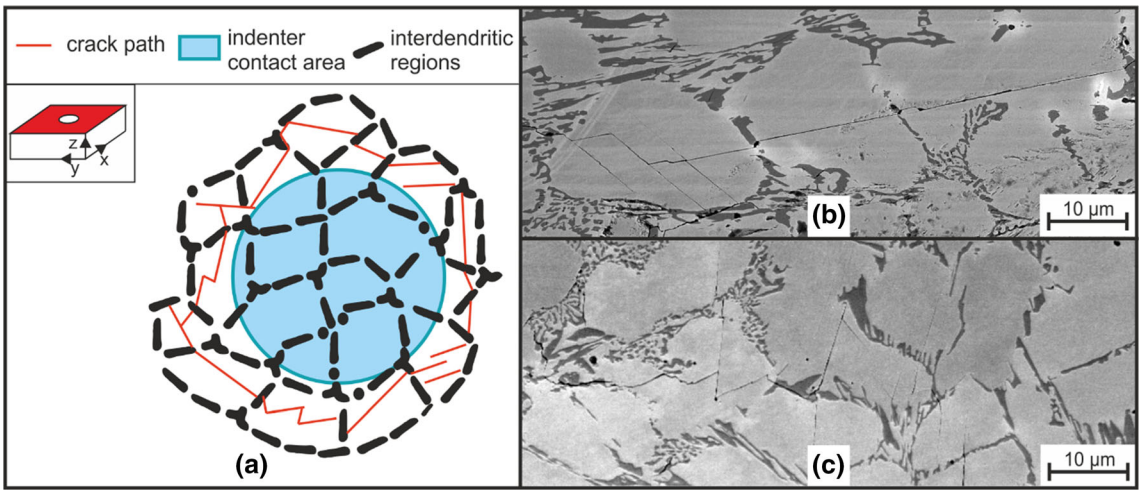

Fig. 7—(*a*) Schematic illustration of the macroscopic crack path in the specimen S6-0Fe (*b*), (*c*) Crack path over the course of several metal matrix cells.

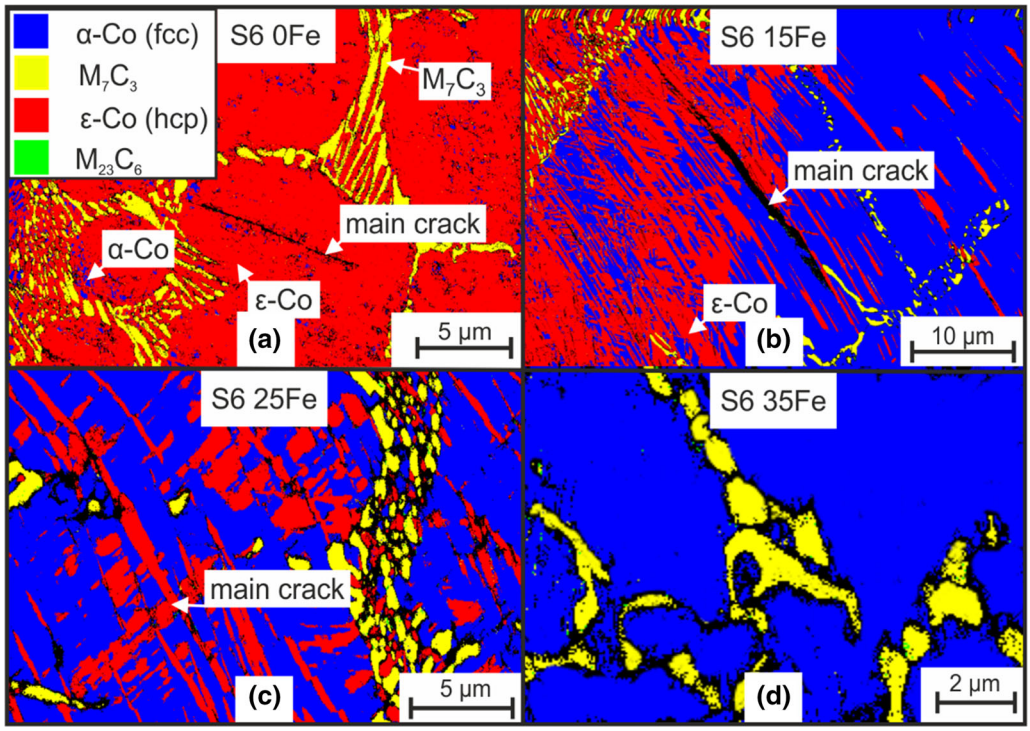

Fig. 8—Phase distribution in the microstructure around the contact area to the indenter after fatigue testing: (*a*) S6-0Fe (*b*) S6-15Fe (*c*) S6-25Fe (*d*) S6-35Fe.

the deformation mechanism towards dislocation slip and deformation twinning was observed (Figure 6 (g)). This observation is in good agreement to the results of previous works, which reported that Co-base alloys with an SFE < 20 mJ/m^2 mainly exhibit SIMT, while SFE values between 20 and 40 mJ/m^2 lead to deformation twinning, and values above 40 mJ/m^2 are associated with dislocation slip.[30–34] There are several reasons why a metal matrix that is deformed by dislocation slip or deformation twinning has a higher resistance against crack growth compared to one that is deformed by SIMT. Zhuang and Langer[24,35] showed on the example of a CoCrMo-alloy that accumulation of stacking faults and ε-Co-formation under cyclic loading cause embrittlement of the metal matrix, as they restrict dislocation slip and, therefore, inhibit the reduction of high stresses at the tip of a fatigue crack by plastic deformation. In the case of this work, the transformation from α-Co to ε-Co reduces the number of slip systems from 12 to 3, which causes a local embrittlement of the metal matrix.

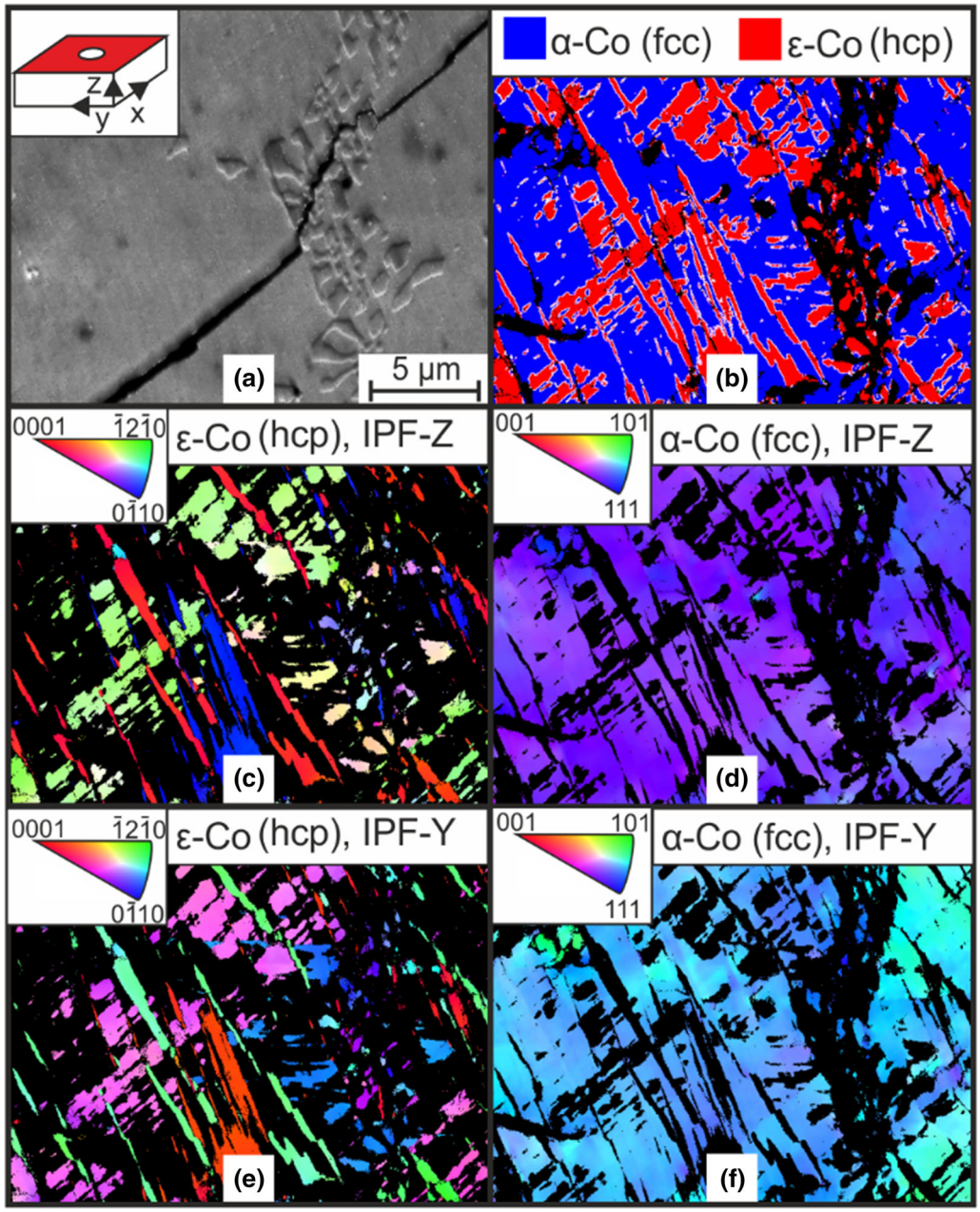

Fig. 9—(*a*) Electron image of the EBSD location on specimen S6-25Fe and coordinate system of the sample. The scanned area is part of the specimen surface that is colored red in the coordinate system. (*b*) Comparison of the crystallographic directions between fcc and hcp areas. Interfaces with a misorientation angle of $< 10°$ from the Shoji-Nishiyama relation are colored white. (*c*) IPF-Z of ε-Co (hcp) (*d*) IPF-Z of α-Co (fcc) (*e*) IPF-Y of ε-Co (*f*) IPF-Y of α-Co (Color figure online).

Also, Chalant[36] pointed out that plastic deformation that is accumulated in deformation twins has high reversibility, which can increase the fatigue life, mainly during the crack initiation period. Especially if crack growth takes place during the unloading period, as is often the case during cyclic compressive loading experiments, the reversibility of deformation could explain the high crack resistance of the metal matrix in the specimen S6-35Fe.

IV. CONCLUSIONS

This work aims to investigate the influence of partial substitution of Co with Fe in the alloy Stellite® 6 on the fatigue behavior. By this Fe-substitution, the stacking fault energy of the fcc Co-base metal matrix increases, which controls the main deformation mechanism under external loading. The main findings can be summarized as follows:

- The stacking fault energy of the metal matrix in the alloy Stellite® 6 can be increased by substitution of Co with Fe. Experimental results give a value of

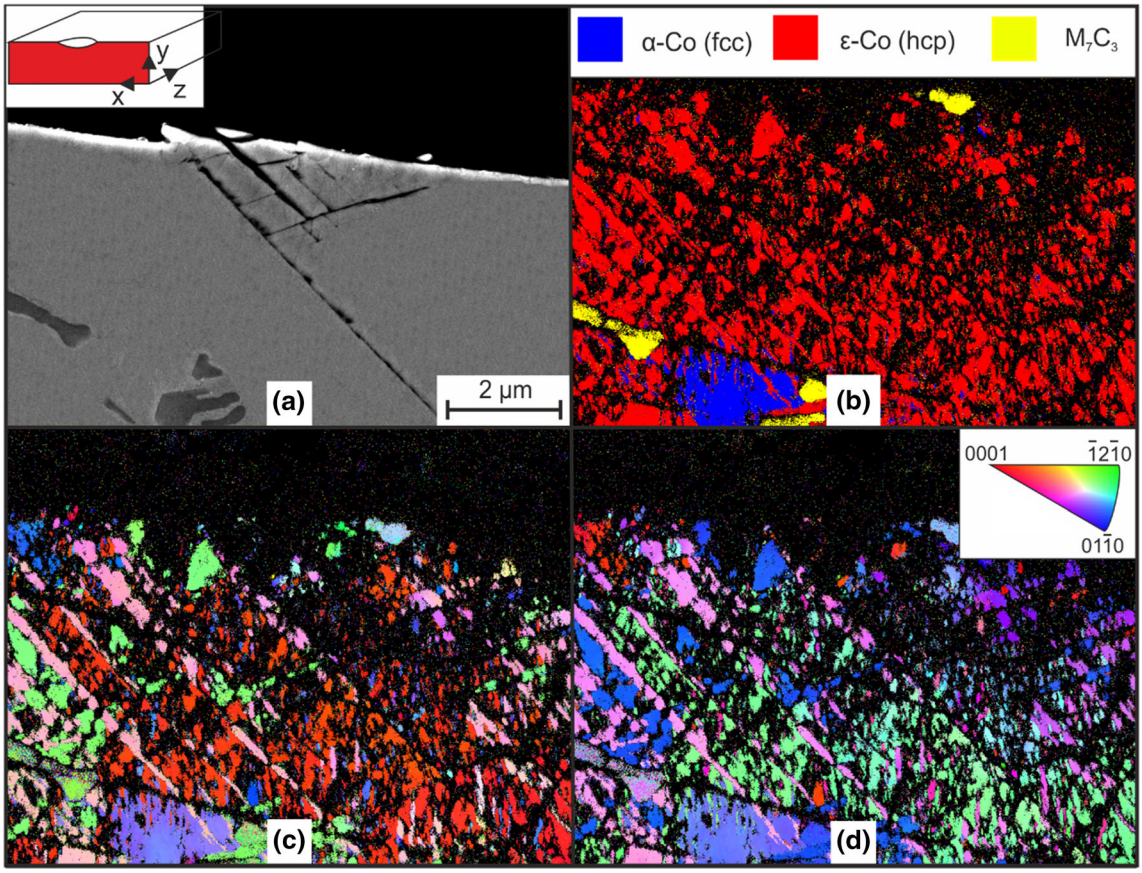

Fig. 10—(*a*) Electron image of the EBSD location on the cut and 90 deg tilted specimen S6-15Fe and coordinate system of the sample. The scanned area is part of the specimen surface that is colored red in the coordinate system. (*b*) EBSD phase contrast (*c*) IPF-Y image (*d*) IPF-Z image (Color figure online).

35 mJ/m^2 for the SFE of Stellite® 6 with 35 mass pct substituted Fe.

- The stacking fault energy of metastable α-Co (fcc) metal matrices with Fe contents of 25 mass pct and below could not be determined experimentally. Thermodynamic calculations indicate a negative SFE of up to − 57 mJ/m^2 for cast Stellite® 6.
- Localized α-Co to ε-Co phase transformation facilitates fatigue crack growth, due to a reduced number of slip systems of the ε-Co phase.
- The fatigue life of Stellite® 6 was increased significantly by substitution of 35 mass pct Co with Fe.
- The primary deformation mechanism of the metal matrix in Stellite® 6 changes from DIMT to dislocation slip and deformation twinning at a Fe content of 35 mass pct

ACKNOWLEDGMENTS

This work was supported by the Deutsche Forschungsgemeinschaft (DFG) in the context of the Collaborative Research Center SFB837 within the subproject C5 (Grant Number 77309832). We sincerely thank the Deutsche Forschungsgemeinschaft for the financial support. The help of the Zentrum für Grenzflächendominierte Höchstleistungswerkstoffe (ZGH) in conducting confocal laser-scanning micrographs is gratefully acknowledged.

FUNDING

Open Access funding enabled and organized by Projekt DEAL.

DATA AVAILABILITY

The raw/processed data required to reproduce these findings cannot be shared at this time as the data also forms part of an ongoing study.

CONFLICT OF INTEREST

On behalf of all authors, the corresponding author states that there is no conflict of interest.

OPEN ACCESS

REFERENCES

1. J. Krell, A. Röttger, and W. Theisen: *Wear*, 2020, vol. 444–445, pp. 2031–38.
2. B.V. Cockeram: *Surf. Coat. Technol.*, 1998, vol. 108–109, pp. 377–84.
3. B.V. Cockeram: *Metall. Trans. A*, 2002, vol. 33, pp. 33–56.
4. H. Berns (ed.) and C. Broeckmann: *Hartlegierungen und Hartverbundwerkstoffe: Gefüge, Eigenschaften, Bearbeitung, Anwendung,* 1st. ed., Springer, Berlin, 1998, pp. 27-52 & 125-54.
5. J. Küpferle, A. Röttger, and W. Theisen: *Wear*, 2017, vol. 390–391, pp. 33–40.
6. L. Brackmann, A. Röttger, S. Weber, and W. Theisen: *Fatigue Fract. Eng. Mater. Struct.*, 2020, vol. 11, pp. 349–65.
7. K. Ishida: *Phys. Solidi A*, 1976, vol. 36, pp. 717–28.
8. L.-Y. Tian, R. Lizárraga, H. Larsson, E. Holmström, and L. Vitos: *Acta Mater.*, 2017, vol. 136, pp. 215–23.
9. D. Yang, C. Hua, S. Qu, J. Xu, J. Chen, C. Yu, and H. Lu: *Metall. Trans. A*, 2019, vol. 50, pp. 1153–61.
10. T. Tisone: *Acta Metall.*, 1973, vol. 21, pp. 229–36.
11. T.L. Achmad, W. Fu, H. Chen, C. Zhang, and Z.-G. Yang: *Comp. Mater. Sci.*, 2016, vol. 121, pp. 86–96.
12. T.L. Achmad, W. Fu, H. Chen, C. Zhang, and Z.-G. Yang: *J. Alloys Compd.*, 2017, vol. 694, pp. 1265–79.
13. R.P. Reed and R.E. Schramm: *J. Appl. Phys.*, 1974, vol. 45, pp. 4705–11.
14. N.C. Popa: *J. Appl. Crystallogr.*, 1998, vol. 31, pp. 176–80.
15. N.C. Popa and D. Balzar: *J. Appl. Crystallogr.*, 2001, vol. 34, pp. 187–95.
16. L. Lutterotti, M. Bortolotti, G. Ischia, I. Lonardelli, and H.-R. Wenk: *Tenth European Powder Diffraction Conference*, Oldenbourg Wissenschaftsverlag, 2007, pp. 125–30.
17. G.B. Olson and M. Cohen: *Metall. Trans. A*, 1976, vol. 7, pp. 1897–1904.
18. W.C. Oliver and G.M. Pharr: *J. Mater Res.*, 1992, vol. 7, pp. 1564–83.
19. W.C. Oliver and G.M. Pharr: *J. Mater Res.*, 2004, vol. 19, pp. 3–20.
20. M.X. Yao, J. Wu, and Y. Xie: *Mater. Sci. Eng. A*, 2005, vol. 407, pp. 234–44.
21. D. Casellas, J. Caro, S. Molas, J.M. Prado, and I. Valls: *Acta Mater.*, 2007, vol. 55, pp. 4277–86.
22. B. Xiao, J.D. Xing, J. Feng, Y.F. Li, C.T. Zhou, W. Su, X.J. Xie, and Y.H. Chen: *Phys. B*, 2008, vol. 403, pp. 2273–81.
23. R.P. Reed and R.E. Schramm: *J. Appl. Phys.*, 1969, vol. 40, pp. 3453–58.
24. L.Z. Zhuang and E.W. Langer: *J. Mater. Sci.*, 1990, vol. 25, pp. 683–89.
25. T. Mitsunobu, Y. Koizumi, B.-S. Lee, and A. Chiba: *Scr. Mater.*, 2014, vol. 74, pp. 52–55.
26. K.V. Werner, F. Niessen, M. Villa, and M.A.J. Somers: *Appl. Phys. Lett.*, 2021, vol. 119, p. 141902.
27. R. Ahmed, H.L. de Villiers Lovelock, N.H. Faisal, and S. Davies: *Tribol. Int.*, 2014, vol. 80, pp. 98–114.
28. X. Sun, S. Lu, R. Xie, X. An, W. Li, T. Zhang, C. Liang, X. Ding, Y. Wang, H. Zhang, and L. Vitos: *Mater. Des.*, 2021, vol. 199, 109396.
29. E. Cabrol, C. Boher, V. Vidal, F. Rezaï-Aria, and F. Touratier: *Wear*, 2019, vol. 426–427, pp. 996–1007.
30. L. Remy: *Acta Metall.*, 1978, vol. 26, pp. 443–51.
31. L. Rémy and A. Pineau: *Mater. Sci. Eng.*, 1976, vol. 26, pp. 123–32.
32. J. Talonen and H. Hänninen: *Acta Mater.*, 2007, vol. 55, pp. 6108–18.
33. Y. Koizumi, S. Suzuki, K. Yamanaka, B.-S. Lee, K. Sato, Y. Li, S. Kurosu, H. Matsumoto, and A. Chiba: *Acta Mater.*, 2013, vol. 61, pp. 1648–61.
34. S. Asgari, E. El-danaf, S.R. Kalidindi, and R.D. Doherty: *Metall. Trans. A*, 1996, vol. 28, pp. 1781–95.
35. L.Z. Zhuang and E.W. Langer: *Metall. Trans. A*, 1989, vol. 20, pp. 99–103.
36. G. Chalant and L. Rémy: *Acta Metall.*, 1980, vol. 28, pp. 75–88.